SiPM-Array Based PET Detectors with Depth-of-Interaction Correction

Dennis R. Schaart, *Member, IEEE,* Herman T. van Dam, Stefan Seifert, Ruud Vinke, Peter Dendooven, Herbert Löhner, *Member, IEEE,* Freek J. Beekman, *Member, IEEE*

***Abstract*–We developed a novel high-resolution detector with intrinsic depth-of-interaction (DOI) correction for PET, based on a position-sensitive silicon photomultiplier (SiPM) array coupled to a monolithic scintillation crystal. The spatial distribution of the scintillation light measured by the SiPM array is used to estimate the entry point of the annihilation photon on the crystal front surface. This approach offers the benefit of intrinsic DOI correction. SiPM arrays furthermore enable integration of these detectors in a MRI device while offering faster response and much higher gain than APDs. Initial characterization of a detector prototype consisting of a 13.2 mm × 13.2 mm × 10 mm monolithic LYSO:Ce^{3+} scintillator and a 4 × 4 SiPM array shows that front surface readout (FSR) of the crystal results in significantly better performance than conventional back-surface readout (BSR). PSFs of < 1.6 mm FWHM were measured at the centre of the detector (uncorrected for the ~0.54 mm FWHM test beam diameter). Hardly any loss of spatial resolution was observed for angles of incidence of up to 45°. Energy resolutions of ~12% were obtained. The timing resolution, measured in coincidence with a BaF_2 detector, equaled 960 ps FWHM.**

I. Introduction

We developed a novel high-resolution detector with intrinsic depth-of-interaction (DOI) correction for positron emission tomography (PET). In this detector a position-sensitive silicon photomultiplier (SiPM) array is used to read out a monolithic scintillation crystal. Upon interaction of an annihilation photon within the crystal, the spatial distribution of the scintillation light measured by the SiPM array is used to estimate the entry point of the annihilation photon on the front surface of the crystal. This is achieved by means of a statistical nearest-neighbor algorithm [1].

Reconstructing the entry point of the annihilation photon offers the benefit of intrinsic DOI correction, allowing for high and uniform system resolution. The use of SiPM arrays furthermore opens up the possibility of integrating these detectors in a MRI device. Compared to avalanche photodiodes (APDs), which are also used in MRI-compatible PET devices [2], SiPMs offer the advantages of faster response and much higher gain.

Manuscript received November 14, 2008. This work was supported in part by SenterNovem under grant no. IS055019.

D. R. Schaart, H. T. van Dam, S. Seifert, and F. J. Beekman are with the Delft University of Technology, Mekelweg 15, 2629 JB Delft, The Netherlands (d.r.schaart@tudelft.nl).

R. Vinke, P. Dendooven, and H. Löhner are with the Kernfysisch Versneller Instituut, University of Groningen, Zernikelaan 25, 9747 AA, Groningen, the Netherlands.

The aim of this paper is to present an initial characterization of a detector prototype consisting of a monolithic LYSO:Ce^{3+} scintillator and a 4 × 4 SiPM array. Two different readout geometries are compared: front surface readout (FSR), in which the SiPM array is placed on the crystal surface facing the radiation source, and conventional back-surface readout (BSR). To our knowledge these are the first results obtained with SiPM-array based monolithic scintillator PET detectors.

II. Materials and Methods

The detector prototype is based on a 13.2 mm × 13.2 mm × 10 mm monolithic LYSO:Ce^{3+} scintillator with optically polished surfaces (Crystal Photonics). The 13.2 mm × 13.2 mm crystal surfaces match with the sensitive area of the SiPM array, which is optically coupled to the crystal using Sylgard 527 dielectric gel. All other faces of the crystal are covered with a highly reflective PTFE reflector (Spectralon). The SiPM array (SensL SPMArray 3035G16) is a 4 × 4 array of 2.85 mm × 2.85 mm active area SiPMs tiled together using flip chip technology on a 550 μm thick white float glass substrate at a pitch of 3.3 mm, see Fig. 1. Each SiPM comprises 3640 Geiger-mode avalanche photodiodes (microcells). The SiPMs were operated at the manufacturer-specified bias voltage of 29.3 V (gain ~10^6).

The blue squares in Fig. 2 show the photo-detection efficiency (PDE) for a single SiPM in the array, as specified by manufacturer (private communication). The solid green line shows the emission spectrum of a 3 mm × 3 mm × 3 mm LYSO:Ce^{3+} crystal (Crystal Photonics), measured using the

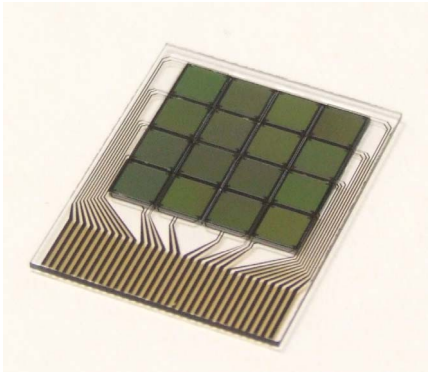

Fig. 1. Photograph showing the 4 × 4 array of SiPMs and the glass substrate of a SensL SPMArray 3035G16. The plastic housing and connector of the device are not shown. Courtesy SensL, Ireland.

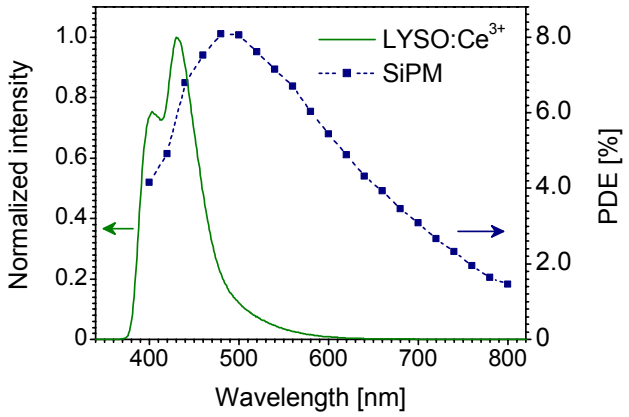

Fig. 2. Comparison of the photo-detection efficiency of a single SiPM of a SensL SPMArray 3035G16 (blue squares, right-hand *y*-axis), which does not include afterpulsing and crosstalk, and the emission spectrum of a 3 mm × 3 mm × 3 mm LYSO:Ce^{3+} crystal (solid green line, left-hand *y*-axis). The effective PDE for the LYSO:Ce^{3+} emission spectrum equals 6.0%.

method described in [3]. The effective PDE (i.e., weighted by the LYSO:Ce^{3+} emission spectrum) equals 6.0%.

Spatial resolution measurements were performed in a slightly upgraded version of the measurement setup described in [1]. Briefly, the detectors are contained in a light-tight, temperature-controlled box. A test beam of 511 keV photons is defined by placing the detector close to a ∅0.5 mm ^{22}Na source and operating it in coincidence with a second detector placed at a larger distance on the opposite side of the source, consisting of a ∅19 mm × 35 mm BGO crystal coupled to a XP2020 PMT equipped with a 60 mm thick Pb collimator with ∅5 mm aperture. For timing measurements the second detector is substituted by a ∅25.4 mm × 25.4 mm BaF_2 crystal on a XP2020Q PMT. A motorized translation and rotation stage allows for irradiating the detector at different positions and angles of incidence.

The SiPM signals are fed into a 16-channel preamplifier board developed in-house, based on a fast, low-noise preamplifier designed to minimize nonlinearity due to SiPM impedance variations. The design and characteristics of these preamplifiers are reported in [4].

The preamplifier signals are fed into a CAEN N568BB 16-channel spectroscopy amplifier operated at a shaping time of 0.2 µs. A CAEN V785 multichannel peak-sensing ADC is used to record the pulse height of each SiPM channel for each event. Time pickoff is performed on a sum signal obtained by means of a high-bandwidth summing amplifier on the preamplifier board, using an Ortec 454 timing filter amplifier (TFA) and an Ortec 935 CFD.

The statistical algorithm used to estimate the entry points of the annihilation photons [1] is summarized in Fig. 3. First, reference data are collected by irradiating the detector with 511 keV photons at a series of known positions and angles of incidence, and recording the light distributions of n_{ref} reference events at each position and angle of incidence. The entry point of an unknown annihilation photon is subsequently estimated by calculating the sum-of-squared-differences of its

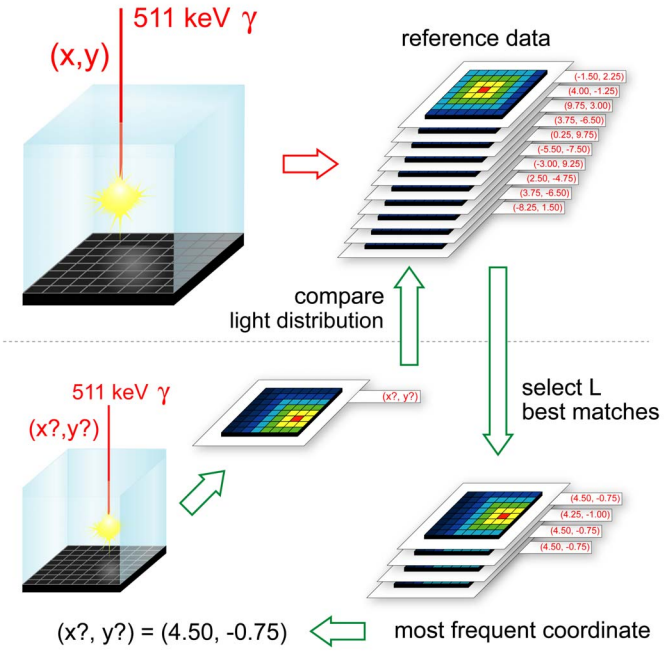

Fig. 3. Statistical nearest-neighbor algorithm used to estimate the entry point of the annihilation photon on the front surface of the crystal from the scintillation light distribution measured by the position-sensitive SiPM array. See text for explanation.

light distribution with those of all events in the reference set recorded at the appropriate angle of incidence. A subset of the reference data consisting of the L closest matches ('nearest neighbors') is selected, and the most frequently occurring entry point within this subset is assigned to the unknown event.

In the present experiments, reference events were recorded at a rectangular, equidistant grid of reference beam positions, having a pitch of 0.25 mm and covering the entire 13.2 mm × 13.2 mm front surface of the crystal at perpendicular incidence. At non-perpendicular incidence, the same reference grid was used so that the lateral crystal surface facing the beam was included in the measurement. The reference events were also used as test events, using the leave-one-out method described in [1]. All measurements were conducted at 24 ± 1 °C, with temperature variations of less than ± 0.2 °C during each measurement. The energy threshold (applied to the sum of the 16 SiPM signals) was set to ~120 keV unless mentioned otherwise.

Measurements were performed in two different readout geometries: front surface readout (FSR), in which the SiPM array is placed on the crystal surface facing the test beam, and conventional back-surface readout (BSR), see Fig. 4. This figure also indicates the coordinate system used to define the annihilation photon entry point. It is noted that FSR is possible without significantly disturbing the annihilation photon beam since the SiPM array is very thin and made of low-Z materials only.

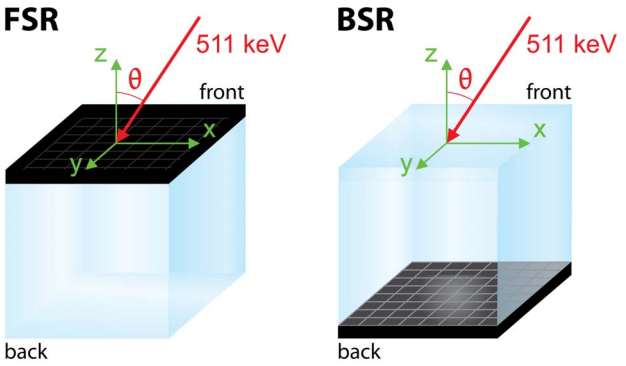

Fig. 4. Readout geometries studied in this work. The left-hand image illustrates the front surface readout (FSR) geometry in which the SiPM array is placed on the crystal front surface. The right-hand image illustrates conventional back-surface readout (BSR). The coordinate system used to define the annihilation photon entry points is also shown. The red arrow indicates an annihilation photon incident on the crystal front surface at an angle θ.

III. Results

The method used to measure the spatial resolution of the detector in principle allows us to derive the detector PSF (i.e., the two-dimensional histogram of the differences between the true and estimated annihilation photon entry points) at each point of the reference grid. However, the number of events L recorded at each point is limited, resulting in considerable statistical fluctuations if the histogram is determined for one such point only. As the PSF is approximately constant over the central area of the detector, the data measured at the central 3.3 mm × 3.3 mm of the detector was therefore combined into a single histogram so as to derive the detector PSF at the detector center with improved statistics.

Fig. 5 shows the corresponding result obtained in FSR geometry. The full width at half maximum (FWHM) and the full width at tenth maximum (FWTM) of this PSF are shown in Table I. It is emphasized that these result still contain the influence of the ~0.54 mm FWHM diameter test beam. Furthermore, these values were obtained with a relatively low energy threshold of ~120 keV. Interestingly, increasing the energy threshold to ~400 keV, so that only full-energy events are selected, hardly influences the results (difference < 1%).

In a further series of measurements the spatial resolutions obtained with different readout geometries and at different angles of incidence were compared. In these measurements the ^{22}Na point source had to be placed at a larger distance from the detector to allow the detector to rotate without touching the source. This results in a larger test beam diameter (~0.64 mm FWHM) and, therefore, slightly worse spatial resolutions. However, this was necessary to keep the beam diameter constant in this series of measurements.

The results of these measurements were analyzed by combining the data measured over the entire measurement grid into a single two-dimensional error histogram. The result, which we will denote as the 'average detector PSF,' can be seen as a measure of the overall detector performance.

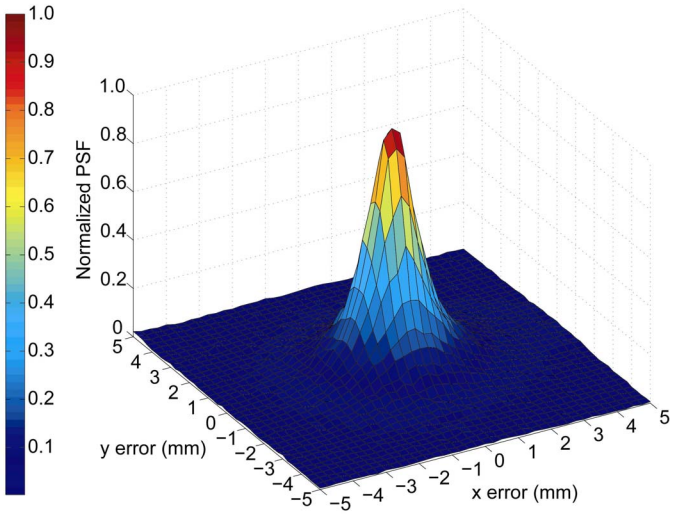

Fig. 5. Detector PSF measured at the detector center at normal incidence with n_{ref} = 1000 and L = 750. Not corrected for the ∅ ~ 0.54 mm FWHM test beam.

TABLE I
FWHM AND FWTM OF THE DETECTOR PSF AT THE DETECTOR CENTER AT NORMAL INCIDENCE. RESULTS ARE NOT CORRECTED FOR THE ∅ ~0.54 MM FWHM TEST BEAM.

PSF cross-section	FWHM (mm)	FWTM (mm)
x-direction	1.58	4.06
y-direction	1.56	4.23

TABLE II
FWHM AND FWTM IN THE X-DIRECTION OF THE AVERAGE DETECTOR PSF AT NORMAL INCIDENCE, MEASURED IN FSR AND BSR GEOMETRIES. NOT CORRECTED FOR THE ∅ ~0.64 MM FWHM TEST BEAM.

Readout geometry	FWHM (mm)	FWTM (mm)
Front surface readout (FSR)	1.86	4.68
Back surface readout (BSR)	2.21	5.33

The spatial resolutions obtained with the FSR and BSR geometries are compared in Table II. FSR appears to perform considerably better than BSR. The same trend was found in previous experiments performed with monolithic PET detectors based on APD arrays [5]. The effect is attributed to the fact that more than 60% of the annihilation photons are absorbed in the front half of the crystal. These events occur closer to the SiPM array in FSR geometry. The corresponding entry points are therefore estimated more accurately than in BSR geometry.

Fig. 6 illustrates how the angle of incidence θ (see also Fig. 4) increases if the annihilation takes place at increasing radial distance from the scanner axis and how this results in increasing parallax errors if the DOI is not corrected for. We tested the intrinsic DOI correction of our detector by studying the average detector PSF, projected onto a plane perpendicular to the line of response (LOR), as a function of θ. In this way,

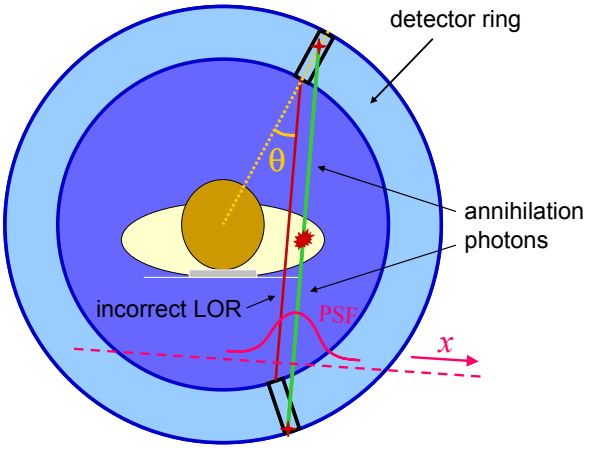

Fig. 6. The angle of incidence θ of the annihilation photons on the detector increases if the annihilation takes place at increasing radial distance from the scanner axis. This results in increasingly incorrect LORs if the DOI is not corrected for. The detector PSF projected onto a plane perpendicular to the LOR, indicated by the pink, dashed line in the figure, corresponds directly to the uncertainty in the position (represented by the *x*-coordinate in this figure) of the true LOR.

the results correspond directly to the uncertainty in the position of the true LOR.

Fig. 7 shows the FWHM and FWTM of the resulting average detector PSF as a function of θ, determined in FSR geometry using the same test beam diameter as in Table II. Hardly any loss of spatial resolution is observed for angles of incidence of up to 45°. Only the FWTM slightly increases with increasing angle of incidence. These results demonstrate the excellent DOI correction of these detectors.

The squares in Fig. 8 show a typical pulse height spectrum measured with 511 keV photons. The horizontal axis corresponds to the sum of the pulse heights of all 16 channels of the SiPM array. A Gaussian fit to the measured data is indicated by the solid red line. The corresponding energy resolution equals 12.2% FWHM at 511 keV.

The solid circles in Fig. 9 show the timing spectrum of the detector, measured in coincidence with a BaF_2 crystal. The solid red line represents a Gaussian fit to the data. The timing resolution equals 960 ps FWHM. Assuming that the contribution of the BaF_2 crystal is negligible, the coincidence timing resolution of 2 of the SiPM-based detectors in coincidence is expected to be $0.96 \cdot \sqrt{2} \approx 1.4$ ns FWHM.

IV. Discussion and Conclusions

A new high resolution PET detector based on a SiPM-array and a monolithic scintillator has been developed. The detector has intrinsic depth-of-interaction (DOI) correction.

The measured spatial resolution is comparable to that obtained with a high-resolution, MRI-compatible PET detector based on a 12 × 12 array of 1.5 mm × 1.5 mm × 10 mm LYSO:Ce^{3+} pixels read out by a 3 × 3 array of SiPMs [6], although it is noted that the position information obtained with the latter type of detector is discrete (identification of the crystal that has been hit), whereas our approach yields (pseudo-)continuous coordinates. While the timing resolution is also very similar (~0.95 ns) for both detectors, the energy

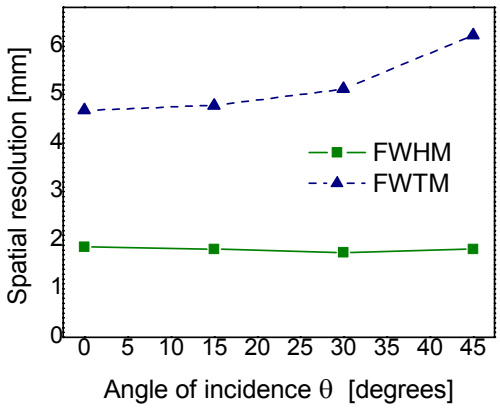

Fig. 7. FWHM and FWTM of the average detector PSF in the *x*-direction as a function of θ. Data were obtained in FSR geometry with $n_{ref} = 250$ and $L = 1000$. Not corrected for the ∅ ~0.64 mm FWHM test beam.

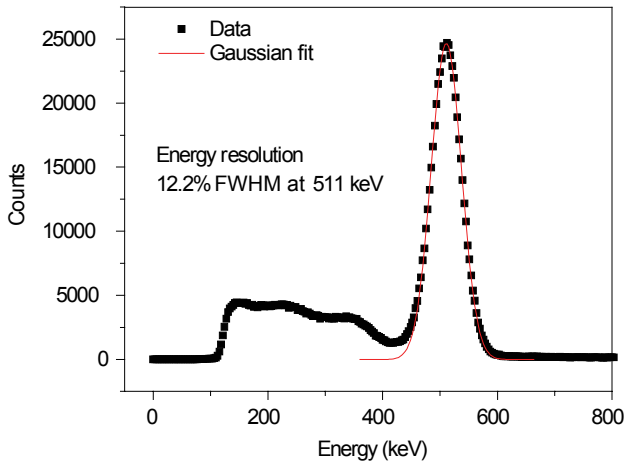

Fig. 8. Pulse height spectrum measured with 511 keV photons (squares). The solid red line indicates a Gaussian fit to the measured data.

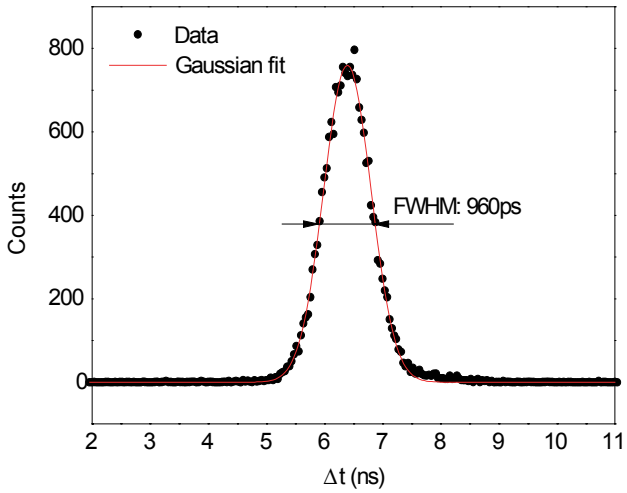

Fig. 9. Coincidence timing spectrum measured in coincidence with a BaF_2 detector using a ^{22}Na source. The solid red line indicates a Gaussian fit to the measured data.

resolution of the monolithic detector is considerably better (~12% FWHM vs. ~22% FWHM). Furthermore, the reduced fraction of dead space in the monolithic approach is expected to result in higher detection efficiency. However, perhaps the most important difference is that the monolithic scintillator detector offers excellent DOI correction, in contrast with the detector based on the pixilated scintillator.

Similar to previous experiments performed with monolithic PET detectors based on APD arrays [5], better spatial resolution is obtained in FSR geometry than in BSR geometry. We have in fact obtained somewhat better spatial resolutions with monolithic scintillator detectors based on APD arrays [1]. The difference is at least partly attributed to the significantly higher PDE of the APD arrays. However, the spatial resolution obtained is inherently limited by the relatively large excess noise factor and dark current of the APD arrays [7]. Due to the relatively low gain of APDs, preamplifier noise may furthermore deteriorate the performance significantly.

Thus, it seems likely that further improvement of the SiPM photo-detection efficiency may eventually result in better spatial resolution than can be obtained with APDs. Moreover, the timing resolution of the present, SiPM-based detector is already considerably better than that of the APD-based detector, while the energy resolution is comparable [1], [7]. We conclude that SiPM arrays are a very promising new type of position-sensitive light sensor for use in PET scintillation detectors.

REFERENCES

[1] M. C. Maas, D. R. Schaart, D. J. van der Laan, P. Bruyndonckx, C. Lemaître, F. J. Beekman, and C. W. E. van Eijk, "Monolithic scintillator PET detectors with intrinsic depth-of-interaction correction," submitted for publication.

[2] M. S. Judenhofer, H. F. Wehrl, D. F. Newport, C. Catana, S. B. Siegel, M. Becker, et. al., "Simultaneous PET-MRI: a new approach for functional and morphological imaging," Nature Medicine 14, 459-465, 2008.

[3] J. T. M. de Haas and P. Dorenbos, "Advances in yield calibration of scintillators," IEEE Trans. Nucl. Sc. 55, 1086-1092, 2008.

[4] S. Seifert, D. R. Schaart, H. T. van Dam, J. Huizenga, R. Vinke, P. Dendooven, H. Löhner, and F. J. Beekman, "A High Bandwidth Preamplifier for SiPM-Based TOF PET Scintillation Detectors," Conference Record of the 2008 IEEE Nuclear Science Symposium and Medical Imaging Conference, Dresden, Germany, 19-25 October, 2008.

[5] M. C. Maas, D. J. van der Laan, D. R. Schaart, J. Huizenga, J. C. Brouwer, P. Bruyndonckx, S. Léonard, Lemaître, and C. W. E. van Eijk, "Experimental characterization of monolithic-crystal small animal PET detectors read out by APD arrays," IEEE Trans. Nucl. Sc. 53, 1071-1077, 2006.

[6] A. Kolb, M. S. Judenhofer, E. Lorenz, D. Renker, and B. J. Pichler, "PET Block Detector Readout Approaches Using G-APDs," Conference Record of the 2008 IEEE Nuclear Science Symposium and Medical Imaging Conference, Dresden, Germany, 19-25 October, 2008.

[7] M. C. Maas, D. R. Schaart, D. J. van der Laan, H. T. van Dam, J. Huizenga, J. C. Brouwer, P. Bruyndonckx, C. Lemaître, and C. W. E. van Eijk, "Signal to noise ratio of APD-based monolithic scintillator detectors for high resolution PET," IEEE Trans. Nucl. Sc. 55, 842-852, 2008.